SOLIDIFICATION OF A CORNSTARCH AND WATER SUSPENSION

SOLIDIFICACIÓN DE UNA SUSPENSIÓN DE MAICENA Y AGUA

S. R. Waitukaitis[†] and H. M. Jaeger

The James Franck Institute and The Department of Physics, The University of Chicago, USA, swaitukaitis@uchicago.edu[†]
† corresponding author

We report on an investigation of the solidification of a cornstarch and water suspension during normal impact on its surface. We find that a finite time after impact, the suspension displays characteristics reminiscent of a solid, including localized stress transmission, the development of a yield stress, and some elastic energy storage. The time dependence of these characteristics depends on the thickness of the cornstarch layer, showing that the solidification is a dynamic process driven by the impacting object. These findings confirm previous speculations that rapidly applied normal stress transforms the normally fluid-like suspension into a temporarily jammed solid and draw a clear distinction between the effects of normal stress and shear stress in dense suspensions.

Se presenta una investigación de la solidificación de una suspensión de maicena y agua durante el impacto normal en su superficie. Se encuentra que, un tiempo finito después del impacto, la suspensión presenta características de un sólido, incluyendo la transmisión local de estrés, el desarrollo de un límite de elasticidad, y el almacenamiento de energía elástica. La evolución temporal de estas características depende del espesor de la capa de maicena, mostrando que la solidificación es un proceso dinámico impulsado por el objeto impactante. Estos resultados confirman anteriores especulaciones sobre la rápida aplicación del estrés normal que transforma la suspensión del estado fluido a un estado atascado temporalmente y establecen una distinción clara entre los efectos de la aplicación del estrés normal y el estrés tangencial en suspensiones densas.

1E**31**

INTRODUCTION

Shear-thickening suspensions, such as a mixture of cornstarch and water, are typically studied in rheometry experiments where shear or tensile stress is measured as a function of the shear rate [1, 2, 3, 4]. The results of these experiments are typically categorized as either reversible or discontinuous. In the former, the change in the suspension's apparent viscosity is small and is generally attributed to the formation of "hydroclusters", small groups of particles interacting through lubrication forces [1, 2, 5, 6]. In the latter, the change in viscosity can appear divergent. This behavior is often associated with forcing the particulate phase across the jamming threshold [3, 4, 7, 8, 9], similar to the creation of "shear-jammed" states in dry granular systems [10]. While these experiments are relevant to the investigation of steady-state shear phenomena, they cannot be expected to apply to large-scale, transient disturbances such as the response during rapidly applied normal stress on the suspension surface. Recent experiments [14, 15] with driven, immersed spheres have shown that applied normal stress can lead to jammed regions of suspension transmitting stress to system boundaries. Even so, these measurements have not given the details of how such jammed regions form. We study this solidification process by investigating the stress transmission through a suspension of cornstarch and water during surface impact. Our results show that the growth of the jammed region is directly linked to the dynamics of the disturbance.

RESULTS AND DISCUSSION

The experimental apparatus is shown in Fig. 1. An aluminum rod ($D = 1.86$ *cm*, $M = 0.368$ *kg*) is allowed to fall-freely or is shot via slingshot into a large tub ($30 \times 30 \times 30$ *cm*) of cornstarch and water suspension. The precise time of impact is determined with the aid of an accelerometer embedded in the rod as well as a high-speed camera, which gives independent access to the instantaneous rod velocity and position. An immersed force sensor simultaneously records the stress transmitted to the container bottom directly below the rod.
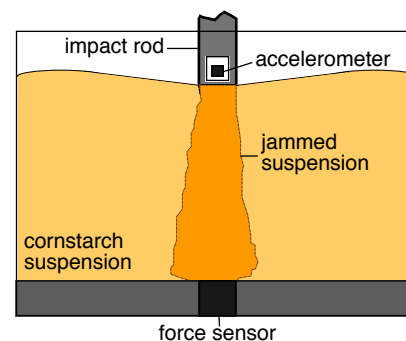

Figure 1: Experimental setup. The impact rod (grey) hits the cornstarch surface, creating a jammed region of suspension (dark orange) which transmits stress to the force sensor at the container bottom.

Fig. 2 shows a typical profile for the force on the rod F_{rod} and the force on the sensor at the container bottom F_b as a function the time after impact with a fill height $H = 10.5$ cm (impact velocity $v_0 = 2.0$ m/s, packing fraction $\phi = 0.49$ and suspending fluid viscosity $\eta = 1.0$ cP). Even for modest impact velocities, this produces an incredibly large force on the rod. In this case, the maximum pressure on the rod face is about 500 kPa and the maximum deceleration ~35 g. The peak force on the rod does not necessarily show temporal correspondence with the peak force on the container bottom, indicating that the force on the rod is not solely a consequence of stress transmission to the container bottom (as is the case for smaller H). For the value of H in Fig. 2, a slow initial buildup of the force measured on the container bottom F_b is followed by an abrupt jump to its maximum value of ~7 N at $t \approx 7.5$ ms. After this, F_b and F_{rod} slowly die away. This is a consequence of both the slowing of the rod as the transmitted force decelerates it and also the concomitant "melting" of the suspension, as is described in the experiments [14] of von Kann et al. Given the area of the sensor is 1.13 cm and assuming the pressure on the bottom is roughly constant, we estimate that the total force on the rod is recovered over an area ~10 cm². This is much smaller than the full area of the container bottom (900 cm²), and if we imagine the stress propagates through the suspension in a cone this corresponds to an angle of about 10º (we remark that this likely underestimates the cone angle given that the pressure is presumably not constant and highest directly below the rod).
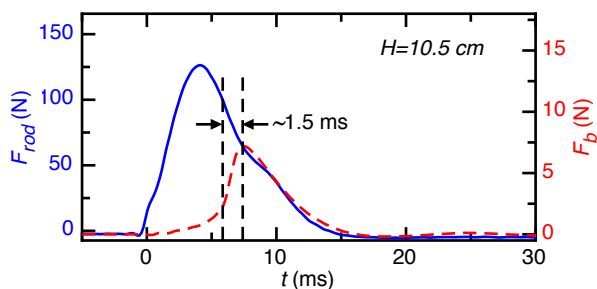

Figure 2: Force on rod F_{rod} (blue curve, left axis) and container bottom F_b (red dashed curve, right axis) vs. time after impact t.

The localization evident from Fig. 2 is the first signature jammed region of suspension transmitting the force on the rod to the container bottom in the manner of a solid. Once this solidified region has formed and reaches bottom, other solid-like behaviors are present. For example, in sufficiently shallow containers and sufficiently high impact speeds, the impacting rod can maintain large amounts of momentum once the growing solid has reached bottom. Rather than yielding and flowing along the bottom, however, the solid compresses, stores energy, and causes the rod to bounce off of the suspension surface. Although it is in principle possible that this energy storage comes from dilation causing grains to poke out from the liquid-air interface [3, 7, 8], we can rule out this possibility by observing that the presence a thin water layer on the suspension surface (~0.5 - 1.0 cm, which prevents particles from interacting with the air-water interface) does not eliminate the bounce. This leads us to conclude that the energy is in fact stored and released by compression of the grains, as

is encountered for the elastohydrodynamic collision between fluid-coated steel spheres in "Stoke's Cradle" experiments [11, 12, 13]. In addition to transmitting stress locally on the container bottom, the jammed region also has a yield stress and can store elastic energy.

We can use shape of the F_b vs. t curves to probe the dynamic details of the solidification process. In particular, the time of the peak can be thought of as the time required for the leading edge of the growing solid to reach the lower boundary. In Fig. 2, for example, knowing that the peak occurs at $t \approx 7.5$ ms and $H = 10.5$ cm allows us to determine that, on average, the suspension solidifies at a rate of ~15 m/s (for $v_0 = 2.0$ m/s). From the sharp upturn to the peak in Fig. 2 (from about 5 - 7 ms), we can make a rough estimate of the width of the leading edge of the solidification region as $\delta \approx v_0 \Delta t \approx 4$ mm. Given that once the solid reaches bottom it must compress a little to develop the peak in F_b, this is likely an overestimate of the front width, but even so it indicates that the front is spatially well-defined in comparison to the size of the solidified region once it hits bottom (~10 cm).
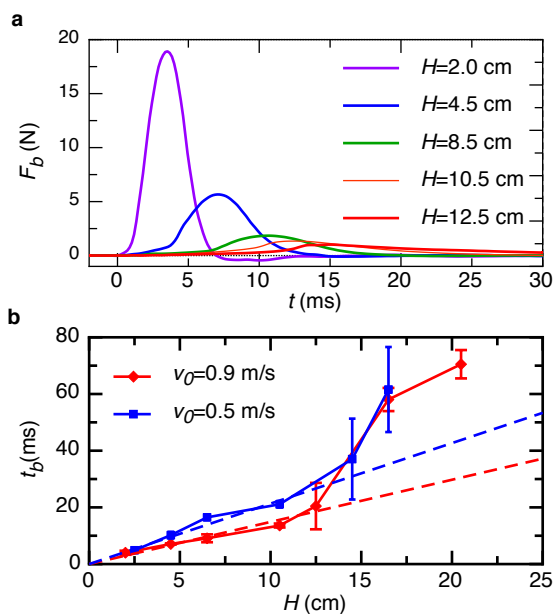

Figure 3: (a) Force on the container bottom (F_b) vs. time for impact at $v_0 = 0.9$ m/s and different fill heights H. (b) Time t_b for the peak in F_b vs. container height H. The error bars show the standard deviations over 3+ individual measurements.

We can gain more insight into this time-dependent solidification by investigating the F_b vs. t curves for different H, as in Fig. 3 (a). As might be expected, the scale of the recovered force decreases monotonically with increasing H and occurs later in time. The weaker force is a result of the decreased speed of the rod when the solid hits bottom as well as the continued spreading of the stress-cone for deeper containers. Plotting the time of the force peak t_b vs. H maps a trajectory of the solid growth, as in Fig. 3 (b). Rather than growing at a constant velocity, the solid develops quickly at first and then slows down. This is reminiscent of the rod trajectory and suggests that the speed of growth is influenced by the speed of the rod (see ref. [16] for example). To test this, we can plot the front

trajectories for different impact speeds, which shows that higher speed impacts produce fronts with faster initial speeds (see the curves for $v_0 = 0.5$ and 0.9 m/s in Fig. 3 (b)). From fitting the portions of these curves before the slow-down we obtain an initial growth rate ~10 times faster than the speed of impact.

At first glance, the dependence of the solidification speed on the rod velocity seems similar to shocks in jammed granular systems [17]. A closer look, however, reveals important differences. The speed at which these fronts propagate seems to scale linearly with the impact speed. In the jammed granular system, two types of propagation are encountered, neither of which scale linearly. In the first case, when the impact speed is low, the front speed is constant and is simply set by the degree to which the grains are pre-compressed before impact (this is essentially sound propagation). In the case of high impact speed, the front speed scales like $v^{1/5}$ as a consequence of the impact causing the already compressed grains to compress further still. These sharp differences can be understood simply by realizing that the system here, unlike the granular system, is *not jammed* before impact; the impact causes it to jam. Given that it is initially unjammed, it cannot support sound propagation through the particle matrix, and it is therefore not surprising that the front speed is not constant but instead depends on the impactor velocity.

CONCLUSIONS

While previous experiments have suggested that under applied normal stress solidified regions of suspension can transmit stress to boundaries, our results give insight into the dynamic details of how this solidification occurs. We show that the solidified region is highly localized, extending over a very small area on the opposing boundary from the impact site. We find that the speed at which the suspension solidifies is set by the speed of the disturbance, with faster solidification occurring for more rapidly applied stress, and that the fronts are spatially well-defined. These results highlight distinct differences between steady-state, shear driven situations and phenomena driven by normal stress, showing that the latter is dominated by the inherently transient character of driving the suspension into the jammed state.

ACKNOWLEDGEMENTS

[1] N. J Wagner and J. F. Brady, Physics Today **62**, 27 (2009).

[2] X. Cheng, J. H. McCoy, J. N. Israelachvili and I. Cohen, Science **333**, 1276 (2011).

[3] E. Brown, N. A. Forman, C. S. Orellana, H. Zhang, B. W. Maynor, D. E. Betts, J. M. DeSimone and H. M. Jaeger Nature Materials **9**, 220 (2010).

[4] E. E. Bischoff-White, M. Chellamuthu and J. P. Rothstein, Rheol. Acta **49**, 119 (2010).

[5] J. F. Brady and G. Bossis, Annu. Rev. Fluid Mech. **20**, 111 (1988).

[6] B. J. Maranzano and N. J. Wagner, J. Chem. Phys. **114**, 10514 (2001).

[7] E. Brown, H. Zhang, N. A. Forman, B. W. Maynor, D. E. Betts, J. M. DeSimone and H. M. Jaeger, Phys. Rev. E **84**, 031408, (2011).

[8] E. Brown and H. M. Jaeger, M. Phys. Rev. Lett. **103**, 086001 (2009).

[9] M. E. Cates, M. D. Haw and C. B. Holmes, J. of Phys: Cond. Matt. **17**, S2517 (2005).

[10] D. Bi, J. Zhang, B. Chakraborty and R. P. Behringer, Nature **480**, 355 (2011).

[11] R. H. Davis and J. -M. Serayssol, J. Fluid Mech. **163**, 479 (1986).

[12] C. Donahue, C. Hrenya and R. Davis, Phys. Rev. Lett. **105**, 034501 (2010).

[13] C. Donahue, C. Hrenya, R. Davis, K. Nakagawa, A. Zelinskaya and G. Joseph, J. Fluid Mech. **650**, 479504 (2010).

[14] S. von Kann, J. H. Snoeijer, D. Lohse and D. van der Meer, Phys. Rev. E **84**, 060401 (2011).

[15] B. Liu, M. Shelley and J. Zhang, Phys. Rev. Lett. **105**, 188301 (2010).

[16] S. R. Waitukaitis and H. M. Jaeger, Nature **487**, 205 (2012).

[17] L. R. Gómez, A. M. Turner, M. van Hecke and V. Vitelli, Phys. Rev. Lett. **108**, 058001 (2012).

FIELD INDUCED MICROPARTICLE STRUCTURE FORMATION IN FLUIDS

FORMACIÓN DE ESTRUCTURAS DE MICROPARTÍCULAS EN FLUIDOS INDUCIDAS POR CAMPO

G. Helgesen[a,b,c †], M. Knaapila[a] A. T. Skjeltorp[a,b,c], H. Høyer[a], J. Cernak[d]

a) Institute for Energy Technology, Kjeller, Norway, geir.helgesen@ife.no[†]
b) Department of Physics, University of Oslo, Norway
c) Centre for Advanced Study at The Norwegian Academy of Science and Letters, Oslo, Norway
d) P. J. Safarik University in Kosice, Slovak Republic
† corresponding author

We review how magnetic and electric fields can be used to create microparticle structures within fluids such as water, oil, polymers, or ferrofluids. The particular arrangement of the electrodes will strongly influence the morphology of the clusters or networks formed, as will also rotating or oscillating fields do. The structure and dynamics of such pattern formation will be described for various types of particles, such as colloidal microspheres, carbon nanoparticles, and metal particles.

Revisamos cómo los campos eléctricos y magnéticos pueden utilizarse para crear estructuras a partir de micropartículas en fluidos como agua, aceite, polímeros o ferrofluidos. El arreglo de electrodos utilizado influye poderosamente la morfología de los "clusters" en las redes que se forman, como también lo hacen los campos rotatorios u oscilatorios. Se describen la estructura y dinámica de la formación de éstos patrones para varios tipos de partículas, tales como microesferas coloidales, nanopartículas de carbono, y partículas metálicas.

PACS: Electrohydrodynamics, 47.65.-d; magnetohydrodynamics in fluids, 47.35.Tv; pattern formation in fluid dynamics, 47.54.-r

INTRODUCTION

Formation of aligned structures within fluids can be obtained by a range of techniques. It is known that mechanical shear in a flowing fluid can align nanoparticles in the fluid into linear chain-like structures [1]. Allowing the fluid to pass above a surface containing protruding micro- or nanostructures leads to similar effects. Static (DC) or oscillating (AC) electric fields may be employed to assemble and align uncharged dielectric particles. Similarly, relatively weak magnetic fields may be used to align dia- or paramagnetic particles.

The motion of charge-neutral particles in a fluid induced by inhomogeneous electric field (AC or DC) is called dielectrophoresis [1]. Magnetophoresis is the similar effect of motion of dia-/paramagnetic particles induced by inhomogeneous magnetic fields [1]. In these two processes a single particle will first be polarized (electrically or magnetically) by the difference in the dielectric constant or the magnetic permeability between the particle and its surrounding carrier fluid. This induced dipole is then pushed away from or attracted toward the source of the field by the field gradient. If another similar particle is placed in the neighborhood of the first, they interact with dipolar forces and will be attracted or repelled depending on the angle between a vector r_{ij} joining their centers and the direction of the external field. Thus, spherical microparticles in an external field interact via the dipolar potential

$$U \propto \sum_{i \neq j} \frac{1}{r_{ij}^3} \left[\sigma_i \cdot \sigma_j - 3 \left(\sigma_i \cdot u_{ij} \right) \left(\sigma_j \cdot u_{ij} \right) \right], \quad (1)$$

where σ_n is the electric dipole moment p_n, or the magnetic moment m_n, of the n-th particle, see Table 1. Here, u_{ij} is a unit vector in the direction of r_{ij}. In addition, any gradient in the external E- or H-field gives rise to a single particle force with a direction that depends only on the difference $\varepsilon_2 - \varepsilon_1$ of the dielectric constants, or $\mu_2 - \mu_1$ of the permeabilities, of the particles and the fluid, respectively. This is outlined in Table 1.

MICROPARTICLE ALIGNMENT IN FLUIDS

Figures 1 (a) and 1 (b) show some examples of dielectrophoretic alignment of microparticles using AC electric fields. Figure 1 (c) shows chain formation of magnetic particles in water in a very weak magnetic field [2] and Fig. 1 (d) shows alignment of nonmagnetic polystyrene spheres dispersed in a ferrofluid [3] in a constant magnetic field $H \approx 800 \, A/m$ [4]. The growth dynamics of such chains follow the cluster-cluster aggregation model [5] where the typical cluster length L grows with time t as $L(t) \sim t^z$ with $z \approx 0.5$ [6]. Also, the distribution of cluster sizes at different times can be rescaled to a common, "universal" functional form [4]. Using an in-plane rotating magnetic field circularly shaped aggregates can be obtained instead of linear strings [7]. Similar structures have been found in experiments

Table I Electric and magnetic force expressions		
External E-field Force on electric dipole p	$F_{edip} = (p \cdot \nabla) E_0$	
Dipole moment of sphere with radius a inside fluid	$p = 4\pi\varepsilon_1 \left(\dfrac{\varepsilon_2 - \varepsilon_1}{\varepsilon_2 + 2\varepsilon_1} \right) a^3 E_0$	Dielectric constants: ε_1 for fluid ε_2 for particles
Dielectrophoretic force on spherical particle	$F_{DEP} = 2\pi\varepsilon_1 K(\varepsilon_1, \varepsilon_2) a^3 \nabla(E_0^2)$	$K(\varepsilon_1, \varepsilon_2) = \left(\dfrac{\varepsilon_2 - \varepsilon_1}{\varepsilon_2 + 2\varepsilon_1} \right)$ Clausius-Mosotti factor
External H-field Force on magnetic dipole m	$F_{mdip} = \mu_0 (m \cdot \nabla) H_0$	
Magnetic moment of sphere inside fluid	$m = 4\pi\mu_1 \left(\dfrac{\mu_2 - \mu_1}{\mu_2 + 2\mu_1} \right) a^3 H_0$	Magnetic permeabilities: μ_1 for fluid μ_2 for particles
Magnetophoretic force on spherical particle	$F_{MAP} = 2\pi\mu_1 K(\mu_1, \mu_2) a^3 \nabla(H_0^2)$	$K(\mu_1, \mu_2) = $ magnetic Clausius-Mosotti factor

and computer simulations of soft magnetic microparticles in uniaxial and biaxial magnetic fields [8] and 3-D networks of strings inside composites have been found using triaxial magnetic fields [9].

PARTICLE ALIGNMENT FOR CONDUCTIVE COMPOSITES

Field-assisted microparticle alignment in polymer dispersions is a convenient and efficient way to create conductive composites with very low loading of conductive fillers. Typical schemes to do this is shown in Fig. 2. A very low volume fraction of conductive nano- or microparticles, such as carbon black (CB), carbon nano-disks and cones (CNC), graphite or metal particles, is dispersed in the polymer and made into a thin ($10 - 100 \ \mu m$) layer on top of a pair of in-plane metal electrodes as shown in Fig. 2 (a) - (c) [10, 11, 12]. The electrodes may be electrically insulated from the polymer dispersion using a plastic foil. Then, an AC voltage is applied between the electrodes and after a few seconds to about a minute, the conductive particles are assembled and aligned into chains by the electric field. These chains may span the gap between the electrodes, thus making a conductive channel in the polymer matrix. The field may alternatively be applied between a bottom

and a top electrode giving rise to conductive chains from one side of the layer to the other, Fig. 2 (d). The polymer can then be cured by heat or UV-light and the conductive chains are locked in place. Finally, the electrodes may be detached from the electrodes (Fig. 2 (c)), creating a free-standing film that is conductive either in-plane or perpendicular to the sheet.

The growth speed depends on the E-field strength and particle concentration as well as the configuration and separation of the electrodes [13]. Typical concentration of filler particles in these conductive films are 0.2 – 1.0 vol-%. This is well below the isotropic percolation limit for conductivity in such mixtures which is typically 2 – 5 *vol-%*. During the alignment, the electrical conductivity of the material rises from the conductivity of the pure polymer $\sim10^{-6}$ *S/m* up to 10^{-3} – 10 *S/m*, depending on the type of filler particle. This conductivity increase takes place during the first minute of alignment and after that there is only a smaller increase as the chains reach their optimal configuration [11, 12]. Some type of chain rearrangement such as merging of two nearby chains and formation of "branched roots" at the electrodes may be seen but this has only a minor influence on the conductivity. After curing of the polymer the conductivity remains fixed. Figure 3 (a) and (b) show the cross section of a sample containing
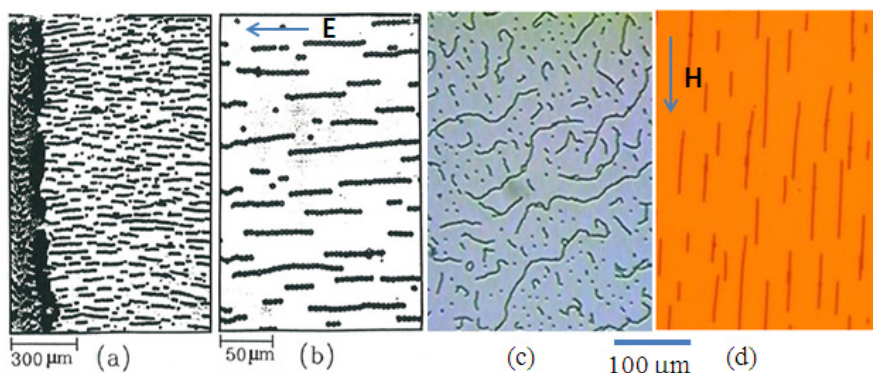

Figure 1: (a) and (b) Electric alignment of 5 μm polystyrene spheres in water at field frequency $f = 1 \ kHz$ and $E = 5 \ V/mm$. (c) Permanent magnetic microbeads in a very weak in-plane magnetic field. (d) Alignment of 4 μm polystyrene microspheres in a ferrofluid.

0.2 *vol*-% CNC with field perpendicular to the layer (Fig. 2 (d)) before and after the alignment process [11].
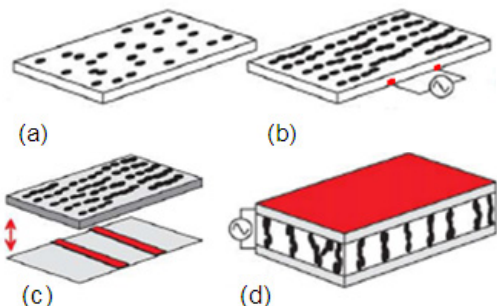

Figure 2: Alignment of particles in thin layers into conductive strings.

An array of electrodes with length 2 *cm* and spacing 100 *μm* and a field with frequency f = 1 *kHz* and strength E = 200 *V/mm* were used to produce the in-plane CNC channels seen in Fig. 3 (c) [10]. Using two needle-shaped gold electrodes on top of a 250 *μm* thick silicon substrate, the single CB string seen in Fig. 3 (d) was formed in about 100 *s* in an AC field with E = 300 *V/mm* [14, 15]. After UV curing, the substrate was bent slightly, resulting in a reversible resistivity change of the string by about 15%. Such strings may be used as strain sensors. No such change was detectable in a similar, isotropically filled sample containing 12 *vol*-% CB. Thus, the piezoresistivity is an effect of the particle alignment. Similar field-structured composites using magnetic fields and Au-coated Ni particles in epoxy have been studied by Martin *et al.* [16]. Such composites may have interesting thermoresistive, piezoresistive, and chemiresistive properties.
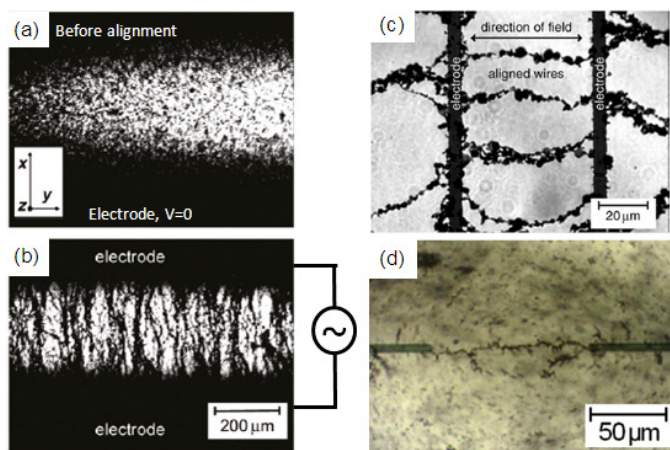

Figure 3: (a) and (b) Cross section of 0.2 *vol*-% CNC in polymer sample before and after field alignment. (c) In-plane alignment of CNC. (d) Single string of CB particles formed between two needle-shaped electrodes.

CONCLUSIONS

Electric or magnetic alignment of particles can be used to create nanostructured conducting composites. Such materials may find applications within the solar energy industry and in electrostatic discharge materials, battery, and sensor applications.

[1] H. Bruus, *Theoretical microfluidics* (Oxford University Press, Oxford, 2008).
[2] G. Helgesen and A. T. Skjeltorp, J. Appl. Phys. **69**, 8278 (1991).
[3] R. E. Rosensweig, *Ferrohydrodynamics* (Cambridge University Press, Cambridge, 1985).
[4] J. Cernak, G. Helgesen, and A. T. Skjeltorp, Phys. Rev. E **70**, 031504 (2004).
[5] T. Vicsek and F. Family, Phys. Rev. Lett. **52**, 1669 (1984).
[6] S. Miyazima, P. Meakin, and F. Family, Phys. Rev. A **36**, 1421 (1987).
[7] J. Cernak and G. Helgesen, Phys. Rev. E **78**, 061401 (2008).
[8] J. E. Martin, E. Venturini, J. Odinek and R. A. Anderson, Phys. Rev. E **61**, 2818 (2000).
[9] J. E. Martin, Composites A **36**, 545 (2005).
[10] M. Knaapila, J. P. Pinheiro, M. Buchanan, A. T. Skjeltorp and G. Helgesen, Carbon **49**, 3171 (2011).
[11] M. Knaapila, O. T. Rømoen, E. Svåsand, J. P. Pinheiro, Ø. G. Martinsen, M. Buchanan, A. T. Skjeltorp, and G. Helgesen, Appl. Mater. Interfaces **3**, 378 (2011).
[12] Matti Knaapila, Henrik Høyer, Eldrid Svåsand, Mark Buchanan, Arne T. Skjeltorp and Geir Helgesen, J. Polymer Science B **49**, 399, (2011).
[13] E. Svåsand, G. Helgesen and A. T. Skjeltorp, Colloids and Surfaces A **308**, 67 (2007).
[14] H. Høyer, M. Knaapila, J. Kjelstrup-Hansen, X. Liu and G. Helgesen, Appl. Phys. Lett. **99**, 213106 (2011).
[15] H. Høyer, M. Knaapila, J. Kjelstrup-Hansen, X. Liu and G. Helgesen, J. Polymer Science B **50**, 477 (2012).
[16] J. E. Martin, R. A. Anderson, J. Odinek, D. Adolf and J. Williamson, Phys. Rev. B **67**, 094207 (2003).

DIPOLAR ORDERING OF CLAY PARTICLES IN VARIOUS CARRIER FLUIDS

ORDENAMIENTO DIPOLAR DE PARTÍCULAS DE ARCILLA EN DIVERSOS FLUIDOS

Z. Rozynek[a†], H. Mauroy[b], R. C. Castberg[c], K. D. Knudsen[b] and J. O. Fossum[a,d‡]

a) Department of Physics, NTNU, Høgskoleringen 5, NO-7491 Trondheim, Norway, rozynek@ntnu.no[†], jon.fossum@ntnu.no[‡]
b) Physics Department, IFE, NO-2027 Kjeller, Norway
c) Department of Physics, University of Oslo, P.O.Box 1048, NO-0316 Oslo, Norway
d) Centre for Advanced Study at the Norwegian Academy of Science and Letters, Drammensveien 78, NO-0271 Oslo, Norway
†, ‡ corresponding authors

We investigate here examples of complexity in composite materials. The objective of the paper is to show that clay particles can be aligned in different hosting media, such as: silicone oil, paraffin-wax, polystyrene and ambient air. The use of an electric field is an easily controllable, non-intrusive manner of inducing such an alignment. Depending on the medium used, a large span in time constants for the orientation and reorganization has been observed. Furthermore, the reorientation may be frozen into the material, thus permanently changing its properties.

Se investigan ejemplos de complejidad en materiales compuestos. El objetivo de este artículo es demostrar que se pueden alinear partículas de arcilla en diferentes medios como aceite de silicona, parafina-cera, poliestireno, y aire. El uso de un campo eléctrico resulta una vía fácilmente controlable y no-intrusiva de inducir el alineamiento. Se observa un amplio rango de constantes de tiempo para la orientación y la reorganización en dependencia del medio utilizado. Aún más, la reorientación puede congelarse en el material, de tal suerte que sus propiedades cambian permanentemente.

INTRODUCTION

Application of an external electric field to a suspension of dielectric clay particles induces polarization of the particles. They will consequently re-orient and aggregate, and this results in the formation of a columnar structure parallel to the electric field direction. The clay particles polarize along their silica sheets, i.e. their stacking direction will be normal to the direction of polarization [1]. The mechanism of the polarization in clays is still under discussion, although one hypothesis is that the intercalated ions and water molecules, which are movable, could play a central role in particle electrical polarization. The resulting induced dipole is attached structurally to the clay particle, and this causes clay particles to reorient and interact, as suggested in [1]. However, recent measurements performed by us indicate that the contribution from the outer surface charges may be dominant, and the particle alignment is then determined by its shape, i.e. so that the longest axis of a single clay particle (or aggregate of particles) will be parallel to the direction of E-field lines [2].

The clay polarization is a rapid process ($< \mu s$) that is followed by a particle re-orientation with a rotation time proportional to the carrier fluid viscosity and inversely proportional to: firstly the difference in the dielectric constants between particle and medium; and secondly the electric field squared (see also [3]). The time scale for particle rotation is in the range of 10^{-3} to 10^{1} s, for E-field between 50 and 2000 V/mm and viscosity of

carrier fluid such as silicone oil between 100 and 500 $mPa{\cdot}s$ [2]. If the particle concentration is high enough, and a minimum critical E-field is applied, chain formation occurs via a particle dipole-dipole interaction [4].

The phenomena described above may be utilized in many different ways and just a few examples are: (i) Electro-rheological fluids (clay particles in silicone oil) in which the so-called liquid-to-solid reversible transition occurs via the application of an external E-field. Such a transition is manifested by changes of ER properties, namely: viscosity, yield stress, storage and loss moduli, etc. [5, 6, 7]. Some examples of application of ER fluids are: fast acting hydraulic valves or clutches [8]. (ii) Nanocomposites (clay particles in polymers), since the aspect ratio of the clay platelets and the interfacial contact area between the clay and matrix are high, the incorporation of small amounts of such inorganic filler into a polymer medium can significantly improve the properties of the resulting polymer/clay nanocomposites. Such nanocomposites can attain a high degree of stiffness and strength [9]. Furthermore, the presence of the dispersed phase results in additional properties, such as flame retardancy or enhanced barrier properties (e.g. gas permeability), when compared to either component [10, 11]. In many situations it is not only the *presence* of the well-dispersed filler but also its *orientational* ordering that may improve certain physical and

chemical properties. The electric-field-induced alignment of clay particles can thus be used to obtain and control a range of the desired material properties.

The above examples have clearly an application-oriented character. However, the focus of our studies is on better understanding of basic physics of such complex systems. Apart from already mentioned hosting media, we also here report for the first time structuring from clays in atmospheric air. The common denominator, for all studied systems, is the clay particle alignment in the presence of an E-field.

SAMPLES

Two types of clay particles, namely laponite (Lp) and fluorohectorite (Fh) are used in the present investigations. The synthetic Lp clay was purchased from Laponite Inc. and the synthetic Fh clay was purchased from Corning Inc. They both belong to the smectite family of clay minerals. Smectites are 2:1 phyllosilicates that possess a net negative charge on the surface of each crystalline layer. Counter ions are located between these lamellar sheets to balance for that charge. Exchangeable cations such as Na^+, Li^+, Ca^{2+}, Mg^{2+}, Cu^{2+} or Fe^{2+} are common. The chemical formulas are: $Na^+_{0.7}[(Mg_{5.5}Li_{0.3})Si_8O_{20}(OH)_4]^{0.7-}$ for Lp clay and $Na^+_{1.2}[(Mg_{4.8}Li_{1.2})F_4Si_8O_{20}]^{1.2-}$ for Fh clay, respectively. They are silicates where a fraction of Mg^{2+} ions is substituted by Li^+ in trioctahedral sites resulting in a negative structural charge [12]. Fluorohectorite has been reported from X-ray data to retain a stacked structure of lamellar particles composed of between 20 and 100 unit layers when dispersed in water, whereas laponite is known to exfoliate into single unit layers in aqueous suspensions [13]. The individual Lp clay particle resembles a disc of average diameter around 30 nm, whereas the size of Fh clay can be as large as several μm.
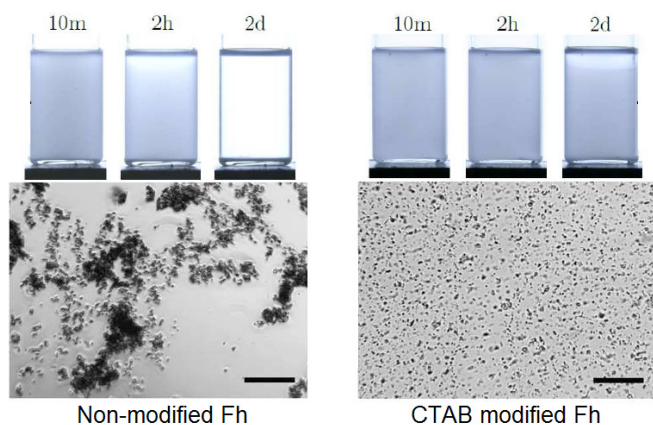

Figure 1: Microscope images of non-modified Fh (left) and organically modified CTAB-Fh (right) clay particles suspended in silicone oil. The length of the bar corresponds to 200 μm. The pictures of the glass vials with samples (top) illustrate the sedimentation dynamics. Adopted from [16].

Clays, in their natural forms, are hydrophilic, or depending on the context they may be referred to as organophobic. When suspended in a non-polar medium, such as silicone oil or polymeric matrix, they tend to form large agglomerates and

consequently sediment (see Figure 1). Addition of surfactants is commonly used to prevent particle agglomeration, which then slows down particle sedimentation, or if the particles are small enough (i.e. magnetic particles in ferrofluids), ensures that they are held in suspension by Brownian motions [14]. Another reason for modifying clays is the ease of uniform dispersion in an apolar polymer matrix. To promote compatibility between the inorganic filler and apolar polymers, it is necessary to chemically modify the inorganic clays by intercalation of organophilic cations, which expand the interlamellar space of the clay, decreasing the interaction among the silicate sheets, and facilitating the diffusion and accommodation of polymeric chains [15].
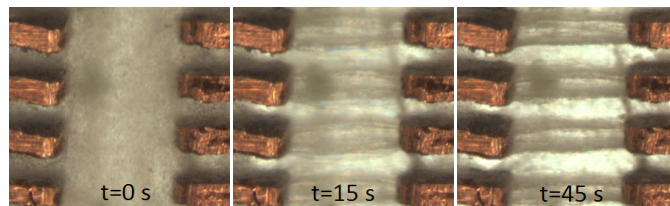

Figure 2: Optical microscopy images of clay/oil suspension without E-field applied (left) and a field of 1000 V/mm (middle and right).

RESULTS

Clays in silicone oil. The preparation of the ER fluid was undertaken by the following procedure. Na-Fh clay powder was crushed with a pestle and mortar, weighed and placed in an oven for 12 h at 110 ^oC. The silicone oil was heated at the same conditions. Subsequently, the clay powder and silicone oil were mixed in glass tubes and sealed. The solutions were then vigorously hand-shaken for 2 min and placed in an ultrasonic bath for 1 h. Before each measurement the samples were hand-shaken again. The clay concentration was approximately 5 $wt.\%$.

Firstly, optical observations were conducted. For that purpose the ER fluid was placed between two electrodes with pre-defined shapes as shown in Figure 2. The gap between the electrodes is roughly 1 mm and the electric field is applied horizontally.
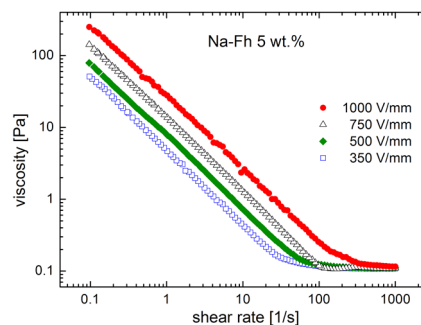

Figure 3: Flow curves for 5 $wt.\%$ clay particles suspended in silicone oil. Different electric field strengths are used, influencing the shear viscosity.

When no E-field is applied, the Fh particles are randomly dispersed into the silicone oil, as shown in Figure 2 (left). Microscopy images of the sample under a DC electric field of 1000 V/mm taken at different times, 15 s and 45 s are shown

1E38

in Figure 2 (middle and right). The formation of column-like structures aligning parallel to the field is clearly observed. Several thin chains are formed first, and these subsequently attract each other resulting in the creation of thicker columns. After a certain time (here several minutes) no major changes in the system are noticeable.
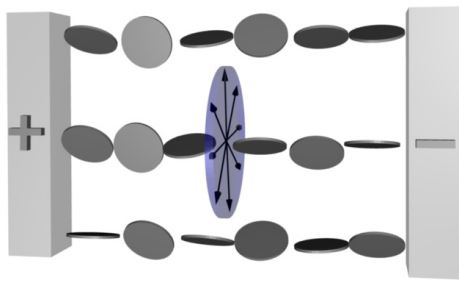

Figure 4: The sketch of the clay alignment in so-called anti-nematic configuration (see text for details).

Imagine now shearing the ER fluid perpendicular to the *E*-field direction. If the *E*-field is not present, the shear viscosity of such a sample (silicone oil and only 5 *wt.*% of clay) is close that of pure silicone oil. However, once the electric field is applied, so that the particles are oriented against the flow, the shear viscosity of a fluid containing clay particles is expected to increase. As the curves in Figure 3 show, this is also what is seen experimentally.

Clays in paraffin-wax. The particular type of paraffin-wax used here has its melting point around 65 ºC and was chosen for two major reasons: (i) optimal melting and crystallization temperatures, providing both easy composite preparation and appropriate stiffness of the composite when in solid form at room temperature; (ii) a relatively non-polar and non-conductive material that can be used as an electrorheological carrier fluid when in the melted state. Fluorohectorite particles (~5 *wt.*%) were dispersed in the melted paraffin and then poured into a custom-made mould with two electrodes. The electric field strength of 500 *V/mm* was applied and kept for a few minutes until the paraffin crystallized and cooled down to room temperature. The solid composite was then investigated using wide-angle X-ray scattering.
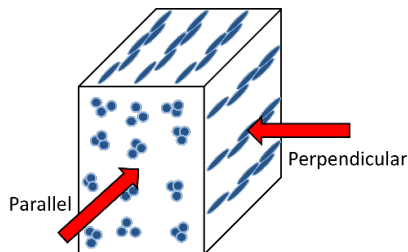

Figure 5: Simple sketch of what the X-ray beam probes in the sample.

When a 2-D X-ray pattern (like those shown in Figure 6) is integrated along the radial direction with a narrow *q*-range (2θ-angle) around the Bragg ring, one obtains a 1-D azimuthal plot which is then fitted using a parametric function. The fitting allows extracting parameters that are further used to calculate the nematic order parameter (S_2) (for details see [17]). This parameter ranges from -1/2 to 1, where 1 indicates perfectly

oriented particles in the nematic configuration, 0 means no orientational order, and finally -1/2 indicates perfectly oriented particles in the anti-nematic configuration [6, 17, 18]. It is expected that the clay particles align in the anti-nematic geometry and the validity of such assumption is tested below.

Several 2-D X-ray images were taken from the same sample at different polar angles, with the rotation axis parallel to the reference direction, which is here the direction of the *E*-field. The nematic order parameter was calculated for four sample positions and the results are presented in Table 1.

Table 1. Nematic order parameter as a function of the polar angle, with the rotation axis parallel to the direction of *E*-field lines.					
Sample rotation	0	30	60	90	Avg
Order parameter	-0.37 ±0.01	-0.35 ±0.01	-0.37 ±0.02	-0.36 ±0.01	-0.36 ±0.01

We observe that the nematic order parameters do not differ significantly from each other indicating that there is no preferential orientation along the polar angle. The arrowed disc shown in Figure 4 represents the plane perpendicular to the *E*-field direction, and that is in fact the average particle stacking direction. The black arrows indicate that clay normals are oriented without any preferred polar direction.
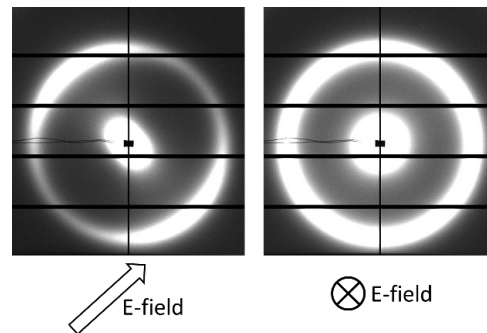

Figure 6: SAXS-patterns from PS/CTAB-Fh with permanently aligned clay chains. Remark: the sample is tilted 45 degrees in the *x-y* plane.

Clays in polystyrene. When aligning clay particles in liquid media the alignment may be lost after a while when the electric field is turned off. An approach to freeze the chain structure was tested by solidifying the matrix while the electric field was applied. The matrix, styrene monomer, polymerizes to give solid polystyrene polymer (PS). A 1 *wt.*% sample of organically modified CTAB-Fh (see [16] for details) was dispersed in styrene monomer and a small quantity of a radical initiator, benzoyl peroxide, was added. The clay/monomer suspension was filled in square shaped glass capillaries, which were sealed with a flame torch. The capillaries were then immersed in an 80 ºC silicone oil bath, and placed between two plate electrodes. The electric field over the electrodes was set to 830 *V/mm*, and the samples were left to polymerize for 7 days. The resulting PS-clay composites were investigated with small angle X-ray scattering (SAXS) at the Dubble beam line at ESRF in Grenoble, France. The samples were probed with the X-ray beam perpendicular and parallel to the direction of clay chains

(see Figure 5). The main ring comes from the characteristic spacing between clay crystalline sheets, and $d_{001} \sim 4$ *nm*. A pronounced anisotropy of the d_{001} peak is seen in Figure 6 (left) due to clay alignment, i.e. on average, particles orient with their stacking direction perpendicular to the *E*-field lines. When probed along the chains the pattern looks isotropic, as shown in Figure 6 (right), since there is no preferential orientation of clay particles along the polar angle (see also [18, 19]).
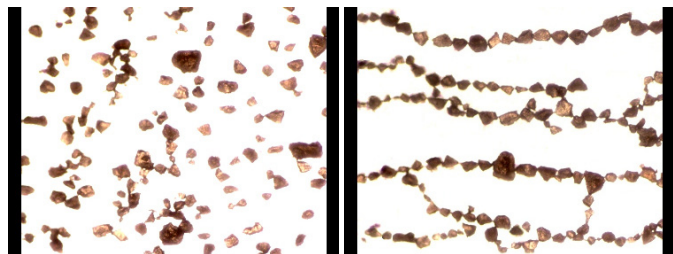

Figure 7: Laponite particle aggregates between two electrodes without *E*-field applied (left) and with an AC *E*-field of 500 *V/mm* (right). The images have been edited to enhance the contrast.

Clays in air. As the final example, we show laponite clay alignment in atmospheric air. Laponite clay powder stored in our laboratory at ~23 ºC and RH in range between 10 and 30 % was used. Such particles normally form aggregates and their sizes can span a few orders of magnitudes reaching a few *mm*. In the present work the size of the aggregates were between 10 and 100 *μm*. Figure 7 shows clay particle aggregates between two electrodes with no *E*-field applied (left) and with an AC *E*-field of 500 *V/mm* (right). The electrodes were kept horizontally and images were taken from above. Clay particles lied on a thin glass substrate, and when the electric field was applied the set-up was gently tapped, lowering the friction as the particles were momentarily suspended in air.

As can be seen, most of the clay particle aggregates align with their longest axis along the *E*-field direction. However, there are several particles disobeying that rule, and these making bridges between individual chains allowing for charge transport. It is possible that the dominant part of the clay polarization occurs only on the clay aggregate surface, not the bulk, i.e. in the clay galleries. However, it is difficult (if not impossible) to draw a firm conclusion on this point, since we deal here with large aggregates. Therefore our future work will be focused on reducing the complexity of the system by working with *single* clay particles, such as vermiculite.

Figure 8: High concentration of laponite particle aggregates between two electrodes with an AC *E*-field of 500 *V/mm* applied. Several particle aggregates (red-color-marked) were not able to re-orient fully with their longest axis along the *E*-field lines due to jamming. This will effectively lower the value of the nematic order parameter.

In Figure 8 we also present structuring from particles in air, but this time the clay concentration is significantly higher. A possible jamming transition may occur where many particles have very little freedom to re-orient (see red-coloured particles). This is an ongoing study and more results are expected in the near future.

CONCLUSION

We have provided examples of recent results from our work on manipulation and orientation of asymmetric particles in external fields. Clay particles are ideal for this purpose due to their inherent large anisotropy and correspondingly high degree of polarizability. When placed in an apolar medium and subjected to an electric field, the particles will orient and organize within a time frame that depends principally on factors such as *E*-field strength and viscosity of the surrounding medium. We have shown how these effects may be induced in various media, with a large span in viscosity, from silicone oil, via polymer matrices to solidified wax, and even air. The clay particles may form chains that span the entire sample volume, thus changing the macroscopic properties of the material. Most notably, there will generally be a large change in the overall rheological behavior, and materials of this kind are therefore highly interesting for applications where the mechanical and structural properties should be manipulated via an electric field.

ACKNOWLEDGEMENTS

[1] J. O. Fossum, Y. Méheust, K. P. S. Parmar, K. D. Knudsen, K. J. Måløy and D. M. Fonseca, Europhys. Lett. **74**, 438 (2006).
[2] R. C. Castberg, Z. Rozynek, J. O. Fossum, K. J. Måløy and P. Dommersnes, work in progress
[3] R. C. Castberg, Z. Rozynek, J. O. Fossum, K. J. Måløy, P. Dommersnes and E. G. Flekkøy, Rev. Cub. Fis. **29**, 1E17 (2012).
[4] J. D. Jackson, *Classical Electrodynamics*, (Wiley 143, 1962).
[5] B. Wang, M. Zhou, Z. Rozynek and J. O. Fossum, J. Mater. Chem. **19**, 1816 (2009).
[6] Z. Rozynek, K. D. Knudsen, J. O. Fossum, Y. Méheust and B. Wang, J. Phys: Condens. Matter. **22**, 324104 (2010).
[7] Y. Méheust, K. Parmar, B. Schjelderupsen and J. O. Fossum, J. Rheol. **55**, 809 (2011).
[8] J. Madeja, Z. Kesy and A. Kesy, Smart Mater Struct. **20**, 105005 (2011).
[9] A. Esteves, A. Timmons and T. Trindade, Quim. Nova **27**, 798 (2004).
[10] S. S. Ray and M. Okamoto, Prog. Polym. Sci. **28**, 1539

(2003).

[11] S. Letaief and C. Detellier, J. Mater Chem. **17**, 1476 (2007).

[12] P. D. Kaviratna, T. J. Pinnavaia and P. Schroeder, J. Phys. Chem. Solids **57**, 1897 (1996).

[13] E. DiMasi, J. O. Fossum, T. Gog and C. Venkataraman, Phys. Rev. E **64**, 061704 (2001).

[14] Z. Rozynek, A. Jozefczak, K. D. Knudsen, A. Skumiel, T. Hornowski, J. O. Fossum, M. Timko, P. Kopecansky and M. Koneracka, Eur. Phys. J. E **34**, 28 (2011).

[15] K. S. Santos, S. A. Liberman, M. A. S. Oviedo and R. S. Mauler, J. Polym. Sci. B: Polym. Phys. **46**, 2519 (2008).

[16] Z. Rozynek, B. X. Wang, J. O. Fossum and K. D. Knudsen, Eur. Phys. J. E **35**, 9 (2012).

[17] Y. Méheust, K. D. Knudsen and J. O. Fossum, J. Appl. Cryst. **39**, 661 (2006).

[18] I. Dozov, E. Paineau, P. Davidson, K. Antonova, C. Baravian, I. Bihannic and L. J. Michot, J. Phys. Chem. B **115**, 7751 (2011).

[19] Z. Rozynek, R. C. Castberg, A. Mikkelsen and J. O. Fossum, work in progress.

VORTEX FLOW AROUND A CIRCULAR CYLINDER NEAR A PLANE

FLUJO DE UN VÓRTICE ALREDEDOR DE UN CILINDRO CERCA DE UN PLANO

M. N. Moura[†] and G. L. Vasconcelos

Departamento de Física, Universidade Federal de Pernambuco, marcelmoura@yahoo.com.br[†]
† corresponding author

The study of vortex flows in the vicinity of multiple solid obstacles is of considerable theoretical interest and practical importance. In particular, the case of flows past a circular cylinder placed above a plane wall has attracted a lot of attention recently. In this case, a stationary vortex is formed in front of the cylinder, in contradistinction to the usual case without the plane where a vortex pair is observed behind the cylinder. In the present work, we apply modern complex analysis techniques to obtain the complex potential for the problem of one point-vortex placed in a uniform stream past a circular cylinder above a plane. A typical streamline pattern is also shown.

El estudio de flujos de vórtices en la vecindad de múltiples obstáculos sólidos es de gran interés teórico y de importancia práctica. En particular, el caso de los flujos alrededor de un cilindro circular colocado encima de una pared plana ha atraído mucha atención recientemente. En este caso, se forma un vórtice estacionario delante del cilindro, en contraposición con el caso habitual sin el plano, donde se observa un par de vórtices detrás del cilindro. En el presente trabajo, se aplican modernas técnicas de análisis complejo para obtener el potencial para el problema de un vórtice puntual colocado en una corriente uniforme alrededor de un cilindro circular colocado encima de un plano. Se muestra un esquema de líneas de corriente típico.

INTRODUCTION

The formation of vortices in viscous flows past cylindrical structures is a problem of considerable theoretical interest and practical relevance for many applications [1]. For example, in the case of a flow past a circular cylinder a pair of counter-rotating vortices forms behind the cylinder at small Reynolds numbers. This vortex pair then goes unstable at higher Reynolds numbers and evolves into a von Kármán vortex street. This system was first studied analytically by Föppl in 1913 [2]. Modelling the vortex flow in terms of point vortices in an otherwise inviscid and irrotational flow, Föppl was able to find stationary configurations for a pair of vortices behind the cylinder and analyze their stability. (Part of Föppl's original stability analysis was however an error, as it has been pointed out by several authors [3, 4].) Because it is amenable to analytical treatment, the point-vortex model is an important tool to study the basic aspects of vortex dynamics in real fluids. In addition, the study of vortex phenomena directly from the Navier-Stokes equation is very costly computationally, which makes the point-vortex model even more attractive.

The problem of vortex flow in the presence of several solid boundaries (obstacles) is much more difficult, and theoretical studies for such cases are more sparse in the literature. One geometry of particular interest is that of a uniform flow past a circular cylinder placed above a planar solid wall, where vortices can form upstream of the cylinder [5]. Here we wish to investigate this problem in terms of a point-vortex model.

More specifically, we consider a point vortex of intensity Γ placed in a uniform stream of velocity U past a circular cylinder of radius s, whose center lies at a distance d from a plane; see Fig. 1. The main objective of the present paper is to derive the complex potential for this system. A typical streamline pattern of the flow will also be presented.
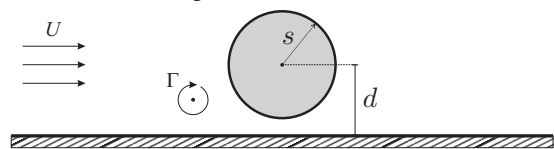

Figure 1: Point vortex in a uniform stream past a circular cylinder above a plane.

Since the fluid domain for the case in study (Fig. 1) is not simply connected (nor can it be reduced to a simply connected region by symmetry arguments), we need to consider conformal mappings between multiply connected domains in order to compute the complex potential for the flow. More specifically, we shall make use of a mathematical formalism recently developed by Crowdy and Marshall [6], which is based on the so-called Schottky-Klein prime function, as discussed next.

METHODOLOGY

We assume that the fluid is inviscid, irrotational, and incompressible, so that the fluid velocity $\vec{v}(x, y)$ is given by the gradient of a potential function: $\vec{v} = \nabla\phi$, where the

velocity potential $\phi(x,y)$ obeys Laplace equation: $\nabla^2\phi = 0$. Our main goal here is to compute the complex potential $w(z) = \phi(x,y) + i\psi(x,y)$, where ψ is the so-called stream function, for the problem illustrated in Fig. 1. To this end, let us introduce the conformal mapping $z(\zeta)$ from an annular region, $r_0 < |\zeta| < 1$, in the auxiliary complex ζ-plane onto the fluid domain in the complex z-plane, where the unit circle $|\zeta| = 1$ is mapped to the plane boundary and the inner circle $|\zeta| = r_0$ is mapped to the cylinder. Furthermore, the points $\zeta = i$ and $\zeta = -i$ are mapped to $z = 0$ and $z = \infty$, respectively; see Fig. 2.
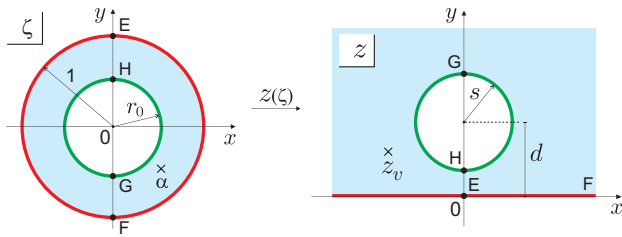

Figure 2: Circular domain in the auxiliary complex ζ-plane (left) and physical domain in the complex z-plane (right).

It is not difficult to see that the function that enacts the desired mapping is given by

$$z(\zeta) = -i\sqrt{d^2 - s^2}\left(\frac{\zeta - i}{\zeta + i}\right), \tag{1}$$

whose inverse is

$$\zeta(z) = -i\frac{z - i\sqrt{d^2 - s^2}}{z + i\sqrt{d^2 - s^2}}. \tag{2}$$

The radius r_0 of the inner circle in the ζ-plane is related to the physical parameters s and d by the following expression:

$$r_0 = \frac{1 - \sqrt{\frac{d-s}{d+s}}}{1 + \sqrt{\frac{d-s}{d+s}}}, \tag{3}$$

as can be easily verified.

Before presenting the complex potential for the problem above, it is instructive to recall [7] that the complex potential for a point vortex of intensity Γ located at position $z = z_v$ (in an unbounded domain) is given by

$$w(z) = \frac{\Gamma}{2\pi i}\log(z - z_v). \tag{4}$$

Similarly, for a vortex in the presence of a cylinder of radius a, the complex potential can be easily obtained by virtue of the Milne-Thomson circle theorem [8], which yields

$$w(z) = \frac{\Gamma}{2\pi i}\log\left[\frac{z - z_v}{z - a^2/\bar{z}_v}\right]. \tag{5}$$

Here the term in the numerator comes from the contribution to the complex potential from the vortex itself, see Eq. (4); whereas the term in the denominator corresponds to the contribution from the vortex image (inside the cylinder), which is necessary to enforce the boundary condition that the

cylinder surface be a streamline of the flow.

For the geometry shown in Fig. 1, where in addition to the cylinder there is an extra boundary (the plane $y = 0$), the circle theorem is no longer of help, and one has to resort to an alternative approach in order to compute the contribution from the infinite set of vortex images (both inside the cylinder and below the plane). In this case, it is more convenient to compute the complex potential in the auxiliary ζ-plane and then transform it back to the z-plane. Indeed, it can be shown [6, 9] that for a point vortex of unit intensity, located at position $\zeta = \alpha$ in a circular domain in the ζ-plane, the complex potential $w_v(\zeta,\alpha)$ is given by

$$w_v(\zeta,\alpha) = \frac{1}{2\pi i}\log\left[\frac{\omega(\zeta,\alpha)}{|\alpha|\,\omega(\zeta,\frac{1}{\bar{\alpha}})}\right], \tag{6}$$

where $\omega(\zeta,\alpha)$ is the so-called Schottky-Klein prime function, which encodes the geometry of the circular domain.

For the particular geometry shown in Fig. 2, the Schottky-Klein prime function $\omega(\zeta,\alpha)$ can be expressed in a simple form:

$$\omega(\zeta,\alpha) = -\frac{\alpha}{C}P\left(\frac{\zeta}{\alpha},r_0\right), \tag{7}$$

where

$$C = \prod_{n=1}^{\infty}\left(1 - r_0^{2n}\right) \tag{8}$$

and

$$P(x,y) = (1-x)\prod_{n=1}^{\infty}\left(1 - y^{2n}x\right)\left(1 - y^{2n}x^{-1}\right). \tag{9}$$

From the definition of the complex potential $w_v(\zeta,\alpha)$ given in Eqs. (6)-(9), one can verify that it satisfies the appropriate boundary conditions in the ζ-plane, namely, that the unit circle and the inner circle are both streamlines of the flow.

The function $P(x,y)$ given in Eq. (9) is related to the first Jacobi theta function ϑ_1, which appears in the theory of elliptic functions [10]. Indeed, it is possible to derive an expression for the complex potential $w_v(\zeta,\alpha)$ entirely within the framework of elliptic functions. The advantage of the method based on the Schottky-Klein prime function is that it can be rather easily extended to two-dimensional vortex flows around an arbitrary number of obstacles. (This general problem is however beyond the scope of the present work.)

Using the complex potential for a vortex of unit intensity given in Eq. (6), it is possible to obtain the complex potential, $w_U(z)$, due to a uniform stream of velocity U past a cylinder above a plane (with no other flow elements). In this case, it can be shown [11] that the corresponding complex potential, $w_U(\zeta)$, in the ζ-plane is given by

$$w_U(\zeta) = -2\pi U i\sqrt{d^2 - s^2}\left(\frac{\partial w_v}{\partial\bar{\alpha}} - \frac{\partial w_v}{\partial\alpha}\right)\bigg|_{\alpha = -i}, \tag{10}$$

with w_v as in Eq. (6). Notice that the derivatives in Eq. (10) are evaluated at the point $\alpha = -i$, which is the point that is mapped to infinity by the conformal map $z(\zeta)$, i.e., $z(-i) = \infty$. In the next section we shall use Eqs. (10) and (6) to construct the complex potential for the vortex flow illustrated in Fig. 1.

RESULTS AND DISCUSSION

The complex potential $w(z)$ for the problem of a vortex of intensity Γ placed at position z_v in a uniform stream in the presence of a cylinder and a plane boundary can be obtained by combining Eq. (10) with Eq. (6), multiplied by Γ. This yields

$$w(z) = w_U(\zeta(z)) + \Gamma w_v(\zeta(z), \zeta(z_v)), \tag{11}$$

where $\zeta(z)$ is the inverse mapping given in Eq. (2). As is well known [7], the velocity field $\vec{v} = (u, v)$ can be found by simply taking the derivative of the complex potential:

$$u - iv = \frac{dw}{dz}. \tag{12}$$

This yields a pair of differential equations for $\dot{x} = u(x, y)$ and $\dot{y} = v(x, y)$, which can be numerically integrated to generate the flow streamlines. It is however more convenient to take an alternative approach, namely, perform a contour plot of the stream function $\psi(x, y)$, which can be easily obtained by taking the imaginary part of the complex potential (11). Each level set $\psi(x, y) = c$, with c being a constant, then yields a streamline of the flow. Figure 3 shows the streamline pattern obtained from the contour plot just described for the case when $U = 1$, $\Gamma = -10$, and the vortex is located at $z_v = -1.5 + 0.5i$.
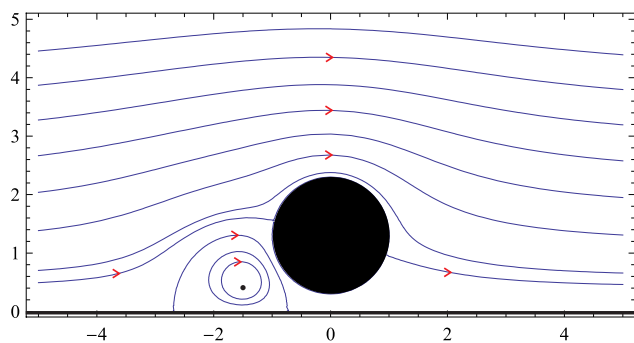

Figure 3: Streamline pattern for the flow studied. The parameters chosen are $\Gamma = -10$, $U = 1$, and $z_v = -1.5 + 0.5i$.

The streamline pattern shown in Fig. 3 displays some interesting features. Of particular interest is the formation of a recirculation zone around the vortex in front of the cylinder. A pattern similar to this was seen in the experiments on flows past a circular cylinder above a plane reported in Ref. [5]. Notice that the recirculation zone acts as an "obstacle" to the oncoming flow, deflecting part of the fluid over the top of

the cylinder and thus reducing the flow though the gap. Note also that far above from the cylinder the streamlines tend to be straight lines, meaning that far away from the cylinder one recovers the uniform flow imposed by the uniform stream, as expected.

CONCLUSIONS

We computed the complex potential $w(z)$ for a point vortex in a uniform stream past a circular cylinder placed above a plane wall. From the imaginary part of $w(z)$, we obtained the stream function of the flow whose level sets yield the streamlines. In particular, we presented the streamline pattern for the case when the vortex is placed upstream of the cylinder —a situation that is of interest to the experiments on viscous flows past a cylinder above a plane recently performed by Lin *et al.* [5]. The next step towards a more complete theoretical understanding of the system is to study the vortex dynamics in this geometry, by allowing the vortex to move with the flow velocity (excluding the vortex own contribution) at the vortex position. This analysis is currently in progress.

ACKNOWLEDGMENTS

[1] B. M. Sumer and J. Fredsøe, *Hydrodynamics around cylindrical structures* (World Scientific, Singapore, 2006).

[2] L. Föppl, Sitzb. Bayer. Akad. Wiss. **1**, 1 (1913).

[3] S. Tang and N. Aubry, Phys. Fluids **9**, 2550 (1997).

[4] G. L. Vasconcelos, M. N. Moura, and A. M. J. Schakel, Phys. Fluids **23**, 123601 (2011).

[5] W. J. Lin, C. Lin, S. C. Hsieh, and S. Dey, J. Eng. Mech. **135**, 697 (2009).

[6] D. G. Crowdy and J. S. Marshall, Proc. R. Soc. A. **461**, 2477 (2005).

[7] P. G. Saffman, *Vortex Dynamics* (Cambridge University Press, Cambridge, 1992).

[8] L. M. Milne-Thomson, *Theoretical Hydrodynamics* (Dover, New York, 1996).

[9] D. G. Crowdy, Theor. Comput. Fluid Dyn. **24**, 9 (2010).

[10] D. G. Crowdy and J. S. Marshall, Phys. Fluids **17**, 056602 (2005).

[11] M. N. Moura, "Vortex motion around a circular cylinder both in an unbounded domain and near a plane boundary," Master's thesis, Federal University of Pernambuco, 2012.

IMPACT DYNAMICS IN "HARD" AND "SOFT" GRANULAR MATTER

DINÁMICA DE IMPACTO EN MATERIA GRANULAR "DURA" Y "BLANDA"

H. Torres[a‡], A. González[a‡], G. Sánchez-Colina[a,b], J. C. Drake[a,b] and E. Altshuler[a†]

a) "Henri Poincarè" Group of Complex Systems, Physics Faculty, University of Havana, 10400 Havana, Cuba, ealtshuler@fisica.uh.cu[†]
b) General Physics Department, Physics Faculty, University of Havana, 10400 Havana, Cuba
‡ contributed equally as first authors.
† corresponding author

Using a wireless accelerometer, we explore the dynamics of penetration of a sphere falling into very light granular matter prepared with different compactions. The duration of the penetration process until the sphere stops is ~30% bigger for less compacted granular matter, while the maximum penetration depth is ~40% bigger in that case. These outputs are quite remarkable, considering that the differences in the filling factors of the two granular media were smaller than 5%.

Utilizando un acelerómetro inalámbrico, exploramos la dinámica de penetración de una esfera que cae sobre material granular muy ligero, preparado con dos compactaciones diferentes. La duración del proceso de penetración hasta que la esfera se detiene es un ~30% mayor para el medio menos compacto, mientras que la penetración máxima para ese medio es un ~40% mayor. Estos resultados son notables, considerando que la diferencia entre ambos factores de llenado es menor del 5%.

PACS: Granular materials rheology, 83.80.Fg; compaction, granular systems, 45.70.Cc; granular materials, 81.05.Rm

INTRODUCTION

Crater formation by impact in granular matter has been a subject of intense research in the last decade [1-7]. There is still debate about the form of the force law against penetration of the impactor, and how it depends on different experimental parameters, such as the density of the impacting object and the granular matter, the impact speed, the roughness and shape of the impactor, etc. Many of the existing reports concentrate in the study of the maximum penetration depth of the impacting object, and the diameter of the resulting crater. "Dynamical" studies, on the other hand, typically record the vertical position of the impactor during the penetration process [5], and only very few record *directly* its acceleration [6, 7].

In this paper, we use a wireless accelerometer to directly measure the acceleration of a sphere falling into extremely light granular matter, in order to find out how the penetration dynamics depend on the level of compaction of the granular medium.

EXPERIMENT

A cylindrical container of 30 *cm* diameter and 26 *cm* depth was filled with expanded polystirene particles of density 0.014 ± 0.002 *g/cc* and diameter distributed between 2.0 and 6.5 *mm*, peaking at 5.8 *mm* [7]. Near the bottom of the container there was a fine horizontal mesh that allowed air to flow upwards injected by a compressor through a hole at the bottom of the system without loosing any granular material. This setup

allowed us to prepare two types of granular matter:

Soft granular matter (SGM): Air was injected from the bottom from zero flow to a maximum, and then decreased back to zero flow (the maximum flow was selected in such a way that it produced visible "turbulence" at the free surface of the grains). The resulting granular medium, had a volume fraction of 0.64 ± 0.01. Using a rotating drum, we found that the maximum angle of stability for SGM was 29.52º ± 0.25º.

Hard granular matter (HGM): First, SGM was obtained. Then, the container was shaken horizontally for 5 seconds (the oscillations were approximately sinusoidal, with a period of 0.225 ± 0.004 *s* and acceleration amplitude of 1.9 ± 0.3 *m/s²*). The resulting volume fraction was of 0.68 ± 0.01, and the maximum angle of stability was 30.29º ± 0.50º.

The impactor consisted in a 3-axis wireless accelerometer mounted into a 4-*cm* diameter ping-pong ball, in such a way that the *z*-axis of the accelerometer was pointing downwards along the vertical direction. The impactor weighted 23 grams (the lower hemisphere was more massive than the upper to guarantee minimal tilting when traveling through the granular media). The accelerometer had a resolution of 0.0001 *g*, and was able to transmit data in real time at 2.4 *GHz* to a USB node on an external PC, at a data point rate of 120 *Hz* [8].

A small magnet was glued to the top of the ping-pong ball, so